Appl Phys B (2012) 107:1075–1085
DOI 10.1007/s00340-011-4802-y

Applied Physics B
Lasers and Optics

Observation of the $v' = 8 \leftarrow v = 0$ vibrational overtone in cold trapped HD^+

J.C.J. Koelemeij · D.W.E. Noom · D. de Jong · M.A. Haddad · W. Ubachs

Received: 9 May 2011 / Revised version: 7 September 2011 / Published online: 14 January 2012

Abstract We report the observation of the hitherto undetected $v' = 8 \leftarrow v = 0$ vibrational overtone in trapped HD^+ molecular ions, sympathetically cooled by laser-cooled Be^+ ions. The overtone is excited using 782 nm laser radiation, after which HD^+ ions in $v = 8$ are photodissociated by the 313 nm laser used for Be^+ cooling. The concomitant loss of HD^+ is detected by the method of secular excitation (Roth et al. in Phys. Rev. A. 74:040501(R), 2006). We furthermore present details of the experimental setup, and we show that results from spectroscopy of $v' = 8 \leftarrow v = 0$ overtones in combination with accurate ab initio calculations may yield a new value for the proton–electron mass ratio with an accuracy of order 1 ppb.

1 Introduction

The molecular hydrogen ion (H_2^+) and its isotopomers (HD^+, D_2^+, HT^+, etc.) are the simplest (one-electron) molecules. As such they are amenable to high-accuracy ab initio level structure calculations, which currently achieve 0.3 ppb accuracy for rovibrational levels in the electronic ground state [1]. The inclusion of high-order quantum electrodynamics (QED) terms in these calculations makes molecular hydrogen ions an attractive target for experiments aimed at tests of QED. With rovibrational-state lifetimes exceeding 10 ms, it has long been recognized that high resolution optical (infrared) spectroscopy should be possible and could provide accurate experimental input. Several experimental studies were undertaken [2, 3] or are currently in progress [4]. Koelemeij et al. achieved an accuracy of 2 ppb on a Doppler-broadened vibrational overtone transition at 1.4 μm in trapped HD^+ molecular ions, sympathetically cooled to 50 mK [3]. For comparison, the highest accuracy achieved in laser spectroscopy of trapped atomic ions is $\sim 1 \times 10^{-17}$ for Al^+ ions sympathetically cooled by laser-cooled Mg^+ ions [5]. It is therefore likely that the experimental accuracy of 2 ppb, currently being the highest achieved for molecular hydrogen ions, may be substantially improved in future experiments.

Accurate results of laser spectroscopy of HD^+ are a goal of interest for the determination of the value of the proton–electron mass ratio, m_p/m_e, and it has been suggested that this may be achieved by combining ab initio theoretical results with results from spectroscopy [2]. The 2010 Committee on Data for Science and Technology (CODATA) recommended value of m_p/m_e has an accuracy of 0.41 ppb. The value of m_p/m_e is largely determined by two separate mass determinations, namely that of the proton relative mass (in atomic mass units [6, 7]) and the electron relative mass [8]. The resulting 0.41 ppb uncertainty stems primarily from the determination of the electron relative mass. To improve on the 2010 CODATA value of m_p/m_e through spectroscopy of HD^+, an accuracy level of about 0.1 ppb for both theory and experiment is required. We are currently setting up an experiment aimed at high-resolution laser spectroscopy of HD^+ vibrational overtones at an accuracy of order 0.1 ppb. In this paper, we report the detection of the hitherto unobserved $v' = 8 \leftarrow v = 0$ vibrational overtone in the $1s\sigma_g$ electronic ground state of HD^+. In Sect. 2, we explain how

J.C.J. Koelemeij (✉) · D.W.E. Noom · D. de Jong · M.A. Haddad · W. Ubachs
LaserLaB, Vrije Universiteit, De Boelelaan 1081, 1081 HV Amsterdam, The Netherlands
e-mail: j.c.j.koelemeij@vu.nl

Present address:
D. de Jong
Erasmus MC-Daniel den Hoed Oncology Center, P.O. Box 5201, 3008 AE Rotterdam, The Netherlands

this transition may be used to provide experimental input to a new determination of m_p/m_e, and present several a priori theoretical considerations relevant to the experiment. In Sect. 3, we will review the experimental setup and procedure, followed by the presentation of the first spectroscopic signals observed in this experiment in Sect. 4. In Sect. 5, we will discuss the potential of this experiment for a new determination of m_p/m_e.

2 Theory

2.1 Determination of m_p/m_e from vibrational resonances in HD^+

The $1s\sigma_g$ electronic ground state of the molecular hydrogen ion supports rovibrational states of nuclear motion. In the most simplified picture of the HD^+ ion in this state, the two nuclei are separated by twice the Bohr radius, a_0, and harmonically bound to each other through the Coulomb attraction by the electron located halfway the two nuclei. It is then readily shown that vibrational states have an energy of order $hcR_\infty\sqrt{m_e/\mu}(v+1/2)$, with v the vibrational quantum number, while the rotational energy is of order $hcR_\infty(m_e/\mu)J(J+1)$ for rotational angular momentum J. Here, R_∞ equals the Rydberg constant, μ is the HD^+ reduced nuclear mass, m_e denotes the electron mass, h stands for Planck's constant, and c is the speed of light. Rotational and vibrational level spacings can be accurately determined by laser spectroscopy, and the value of m_e/μ may be determined by combining spectroscopic results with accurate theoretical calculations. Details about how this may be done are postponed to Sect. 5.

2.2 Energy levels, wavefunctions, and electric dipole moments

Several high-accuracy calculations of the HD^+ level structure and properties have recently been published; see, for instance, [1, 9] and references therein. However, in many of the available theoretical papers no numerical results are presented for $(v=8, J)$ rovibrational states. Since knowledge of the properties of $(v=8, J)$ and other relevant states is required for the design of the experiment, we followed a relatively simple approach to obtain rovibrational energy levels and wavefunctions, electric dipole moments, photodissociation cross-sections and sensitivity coefficients with respect to proton/electron or deuteron/proton mass variation. In principle, our approach works for any state (v, J), except for high-lying states close to the dissociation limit, which are very susceptible to the details and inaccuracy of the model used here.

Figure 1 shows a partial energy level diagram of the HD^+ molecular ion including the electronic ground-state potential, $1s\sigma_g$, and the first electronically excited potential, $2p\sigma_u$. Note that in HD^+ the g/u symmetry quantum labels are only approximately good quantum labels as the nonidentical nuclei introduce g/u symmetry breaking at large internuclear range. Furthermore, HD^+ is an open-shell molecule, which implies that a multitude of spin couplings exist involving the electron spin, proton spin, deuteron spin and electric quadrupole moment, and the molecular rotation. These couplings lead to hyperfine level splittings up to 1 GHz and have been evaluated theoretically with high accuracy [10, 11], but will not be considered in detail here. The potential energy curves shown in Fig. 1 are interpolations of data published by Esry and Sadeghpour, who presented the potential energy as the sum of a nonrelativistic, fully adiabatic curve, and a diagonal nonadiabatic correction [12]. We use these curves to obtain radial wavefunctions of nuclear motion, $\chi_{vJ}(R)$, by numerical solution of the radial Schrödinger equation including the centrifugal term due to the molecular rotation:

$$-\frac{\hbar^2}{2\mu}\frac{\mathrm{d}^2}{\mathrm{d}R^2}\chi_{vJ}(R)+\left[V_i(R)+\frac{\hbar^2 J(J+1)}{2\mu R^2}\right]\chi_{vJ}(R) = E_{vJ}\chi_{vJ}(R). \quad (1)$$

Here, R is the internuclear separation, and $E_{v,J}$ is the rovibrational energy. The functions $V_i(R)$ (with $i=1,2$) are the potential energy curves of the $1s\sigma_g$ and $2p\sigma_u$ states, respectively, shown in Fig. 1. Dipole moment functions $D_1(R)$ and $D_{12}(R)$ used here are taken also from [12], and correspond to the permanent dipole moment of the $1s\sigma_g$ state and the transition dipole moment for electronic transitions between $1s\sigma_g$ and $2p\sigma_u$, respectively. $D_1(R)$ may be used to estimate transition rates achievable in rovibrational spectroscopy, whereas D_{12} is useful for computing cross-sections for the photodissociation occurring in $2p\sigma_u \leftarrow 1s\sigma_g$ transitions.

2.2.1 *Rovibrational line strengths*

Vibrational overtones are generally weak transitions, and when designing an experiment for overtone spectroscopy it is essential to have information on their line strengths. We compute line strengths and Einstein coefficients as follows. Ignoring the spins of the proton, deuteron and electron, and noting that the $1s\sigma_g$ state has zero orbital angular momentum projection onto the internuclear axis ($\Lambda=0$), we express the dipole transition matrix element between two states with quantum numbers (v, J, M) and (v', J', M') as follows [13]:

$$|D_{vv'JJ'MM'q}|^2 = \left|\left\langle JM\mathcal{D}^*_{-q0}(\omega_\mathrm{E})J'M'\right\rangle\right|^2\mu^2_{vv'JJ'}$$

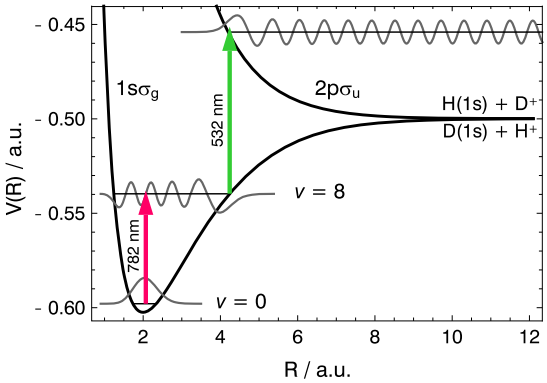

Fig. 1 Potential energy curves of the $1s\sigma_g$ and $2p\sigma_u$ electronic states. Indicated energy values are binding energies of the molecule (in atomic units). Shown also are radial nuclear (vibrational) wavefunctions $\chi_v(R)$ for $v = 0$ and $v = 8$, as well as one dissociating nuclear wavefunction in the $2p\sigma_u$ state. The *red arrow* indicates the 782 nm overtone transition of interest here, and the *green arrow* represents photodissociation by a 532 nm photon

$$= (2J+1)(2J'+1)\begin{pmatrix} J & 1 & J' \\ 0 & 0 & 0 \end{pmatrix}^2 \times \begin{pmatrix} J & 1 & J' \\ -M & -q & M' \end{pmatrix}^2 \mu^2_{vv'JJ'}, \quad (2)$$

with

$$\mu^2_{vv'JJ'} = \left| \int_0^\infty \chi_{v'J'}(R) D_1(R) \chi_{vJ}(R)\, \mathrm{d}R \right|^2. \quad (3)$$

Here, (v, J, M) and (v', J', M') are the quantum numbers of the lower and upper states, respectively, and we assume that the states (v, J) are degenerate in the magnetic quantum number M (corresponding to the projection of $\mathbf{J}$ on the space-fixed z-axis). The dipole matrix element $\mu_{vv'JJ'}$ is a vector oriented along the internuclear axis of the HD^+ molecule. Therefore, in order to evaluate the matrix elements, $\mu_{vv'JJ'}$ needs to be transformed from the molecule-fixed to the space-fixed frame by rotation about the set of Euler angles ω_E, which is implemented through the rotation operator $\mathcal{D}^*_{-q0}(\omega_E)$ in the first factor in (2). In arriving at the second line of (2), we use the fact the projection of J on the internuclear axis is zero. The index $q = -1, 0, 1$ labels the three components of the dipole operator (with respect to the space-fixed frame) in spherical tensor notation.

The squared matrix elements $\mu^2_{vv'JJ'}$ are readily evaluated using the numerical expressions for wavefunctions and dipole moment functions introduced above. We can now calculate the line strength, $S_{vv'JJ'}$, which evaluates to [14]

$$S_{vv'JJ'} = \sum_{M,M',q} |D_{vv'JJ'MM'q}|^2 = \max(J, J')\, \mu^2_{vv'JJ'}. \quad (4)$$

From the line strength, Einstein coefficients for spontaneous emission, absorption, and stimulated emission ($A_{vv'JJ'}$, $\overline{B}_{vv'JJ'}$ and $B_{vv'JJ'}$, respectively) may be obtained using the relations [14]

$$A_{vv'JJ'} = \frac{2\omega^3_{vv'JJ'}}{3\epsilon_0 hc^3} \frac{S_{vv'JJ'}}{2J'+1}, \quad (5)$$

$$B_{vv'JJ'} = \frac{\pi^2 c^3}{\hbar \omega^3_{vv'JJ'}} A_{vv'JJ'}, \quad (6)$$

$$\overline{B}_{vv'JJ'} = \frac{2J'+1}{2J+1} B_{vv'JJ'}. \quad (7)$$

These expressions have been used to obtain spontaneous lifetimes and overtone excitation rates, and the relative accuracy of the matrix elements $\mu_{vv'JJ'}$ is believed to be better than 10^{-3} [15]. This is verified here by comparing the matrix elements with those presented by Bakalov et al. for transitions $v' \leftarrow v$ with v', v ranging from 0 to 4 [16], as well as with those given by Colbourn and Bunker [17]. The results of Bakalov et al. are based on high-accuracy nonrelativistic variational wavefunctions of HD^+, and may be considered to be exact. The values presented by Colbourn and Bunker are based on a Born–Oppenheimer description which does not take g/u symmetry breaking into account, in contrast to the approach presented here. To compare these results, matrix elements for $(v' = 1, J' = 3) \leftarrow (v = 0, J = 2)$ and $(v' = 4, J' = 3) \leftarrow (v = 0, J = 2)$ are listed in Table 1. The agreement of the values calculated here with those of Bakalov et al. is excellent and well within the specified inaccuracy of the former. The values of Colbourn and Bunker, however, differ at the level of 3×10^{-3}. This has been attributed to the fact that Colbourn and Bunker did not take g/u symmetry breaking into account [15].

2.2.2 *Photodissociation cross-sections*

In previous HD^+ spectroscopy experiments, $(1 + 1')$ resonance-enhanced multiphoton dissociation (REMPD) was used to detect rovibrational transitions [3, 18]. In this scheme, the first photon induces the rovibrational excitation within $1s\sigma_g$, whereas the second photon induces an electronic transition to the continuum of dissociating states in the repulsive part of the $2p\sigma_u$ potential. As we are interested in detecting the hitherto unobserved $v' = 8 \leftarrow v = 0$ overtone by $(1 + 1')$ REMPD, it is mandatory to obtain photodissociation (PD) cross-sections as a function of photon energy in order to find a suitable wavelength for the second photon. PD cross-sections may be obtained following the approach by Dunn, who treated the case of H_2^+ and D_2^+ in the Born–Oppenheimer approximation [19]. The same strategy was employed by Tadjeddine and Parlant, who calculated PD cross-sections also for HD^+ [20]. Here we follow the same procedure[1] for HD^+, but using the wavefunctions ob-

[1] Since this strategy takes g/u symmetry breaking into account, the results may be expected to be more accurate. However, a thorough assessment of the accuracy is beyond the scope of this work.

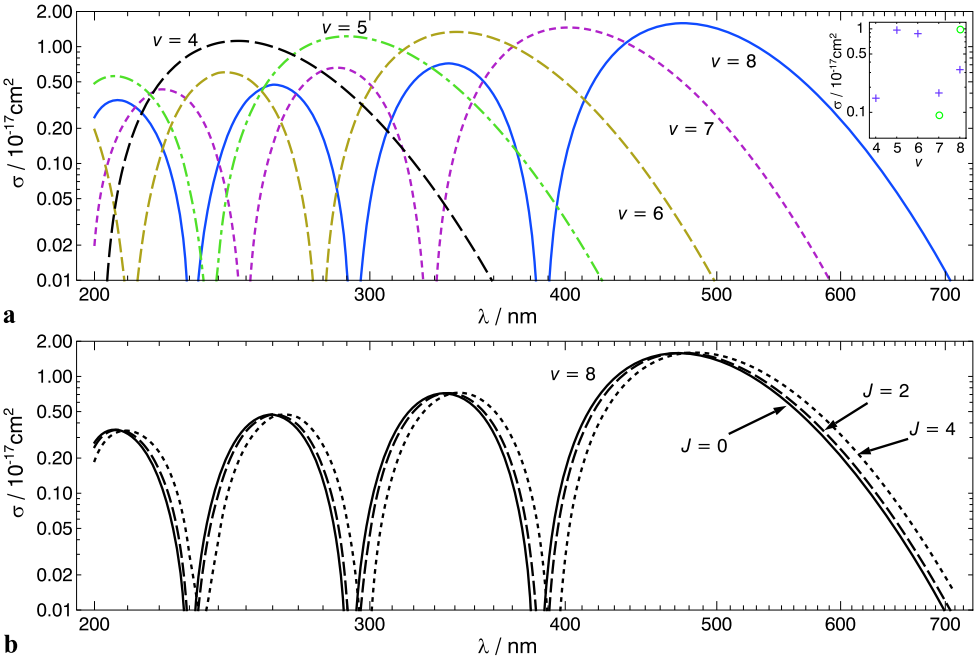

Fig. 2 (**a**) PD cross-sections for various vibrational states v versus the wavelength, λ, of the dissociating photon. For all curves the rotational quantum number $J = 2$. The cross-sections are strongly modulated by Franck–Condon oscillations. *Inset*: cross-sections for various vibrational states by photons of wavelength 313 nm (*crosses*) and 532 nm (*circles*). (**b**) PD cross-sections for $v = 8$ and various J

Table 1 Matrix elements $\mu_{vv'JJ'}$ for various rovibrational transitions $(v', J' = 3) \leftarrow (v = 0, J = 2)$ in units of Debye. Here the notation $[n]$ stands for $\times 10^n$. The results of Bakalov et al. shown here were converted from their original form using (4)

	$v' = 1$	$v' = 4$	$v' = 8$
Colbourn & Bunker [17]	7.799[−2]	−7.6[−4]	
Bakalov et al. [16]	7.8191[−2]	−7.6314[−4]	
This work	7.820[−2]	−7.636[−4]	2.808[−5]

tained from (1) and the electronic transition dipole moment $D_{12}(R)$. Following Dunn, the PD cross-section (in m^2) may be approximated as

$$\sigma_{vJ}(E) = \frac{4\pi\epsilon_0 h}{3m_e c}\sqrt{\frac{\mu_{HD^+}}{\mu_{H_2^+}}}\frac{E}{\sqrt{E_f}} \times \left|\int_0^\infty \chi_{E_f J'}(R) D_{12}(R) \chi_{vJ}(R)\,\mathrm{d}R\right|^2. \quad (8)$$

Here, E equals the photon energy, and E_f is the kinetic energy of the dissociation products above the $2p\sigma_u$ dissociation limit. Following Dunn's convention, all energies in (8) are expressed in Rydbergs, while the dipole matrix element is expressed in atomic units. We ignore PD due to transitions to continuum states *within* $1s\sigma_g$, mediated by the permanent nuclear electric dipole moment, which we estimate to contribute to the cross-section only below the 10^{-3} level. Figure 2(a) displays PD cross-sections versus photon wavelength for the range of vibrational states $v = 4$–8, whereas Fig. 2(b) illustrates the variation of PD cross-sections with the molecular rotation. We verified the validity of our calculations by comparing with experimental and theoretical results for HD^+ [20, 21], as well as by re-evaluating the case of H_2^+ and comparing the results with those by Dunn [19] and Kilic [22].

3 Experimental approach

With the experimental setup described previously in [3], spectroscopy of a $v' = 4 \leftarrow v = 0$ overtone at 1.4 μm was demonstrated with an accuracy of 2 ppb, limited by signal-to-noise and Doppler broadening due to residual motion of the trapped HD^+ molecular ions, which were sympathetically cooled by laser-cooled Be^+ ions. In the experimental setup presented here, the same methods for trapping and cooling HD^+ are used. We nonetheless believe that with our setup detrimental effects of signal noise and Doppler broadening may be reduced substantially so as to improve the accuracy to 0.5 ppb for a single rovibrational line (Sect. 5).

3.1 Laser systems

3.1.1 Preliminary considerations

Moss tabulated theoretical HD^+ rovibrational level energies with an accuracy <0.001 cm^{-1} [23]. From these tables, we

find that the $(v' = 8, J') \leftarrow (v = 0, J)$ overtones require excitation wavelengths in the range 782–807 nm for $J = 0, 1, \ldots, 5$ and $J' - J = \pm 1$. This wavelength range is covered by commercially available continuous-wave (CW) titanium:sapphire (Ti:S) lasers. However, the $v' = 8 \leftarrow v = 0$ overtones are expected to be very weak, and one may question whether the irradiance obtainable with such a laser system is sufficient to achieve an appreciable transition rate. Here it is useful to make an comparison with the experimental setup for spectroscopy of the $(v' = 4, J' = 3) \leftarrow (v = 0, J = 2)$ overtone described by Koelemeij et al., who focused 170 μW of laser power at 1.4 μm to a beam waist (or spot size) of 200 μm, and achieved sufficiently strong signals after 6 s of REMPD [3]. From (7) we obtain Einstein coefficients $\overline{B}_{vv'JJ'}$ for $v' = 8 \leftarrow v = 0$ overtones which are smaller than those for $(v' = 4, J' = 3) \leftarrow (v = 0, J = 2)$ by a factor of 400–1000. Thus we conclude that ∼200 mW of power focused to 200 μm spot size should suffice, which may be readily achieved using a Ti:S laser. The excitation rate may also be readily estimated using (7), taking Doppler broadening and the linewidth of the excitation laser (relative to the linewidth of the rovibrational transition) into account. For HD^+ ions at 10 mK, we find an excitation rate for $v' = 8 \leftarrow v = 0$ of 35 s^{-1}, given a laser linewidth of 100 kHz.

Another remaining open question is which laser wavelength and irradiance must be used for PD of the $v = 8$ state. Koelemeij et al. used 1 mW of 266 nm laser radiation, focused to 100 μm spot size, to efficiently dissociate $v = 4$. From the curves shown in Fig. 2(a) it can be seen that the corresponding PD cross-section is 0.9×10^{-17} cm^2. From the curve for PD of $v = 8$ it is seen the cross-section for 532 nm radiation is slightly larger. 1 mW of 532 nm may be obtained by picking off a small amount of power from the 532 nm laser used to pump the Ti:S laser system mentioned above. From the same PD curve it is also seen that the cross-section for PD at 313 nm is about three times smaller, so some PD may be expected to occur due to the 313 nm laser used for Be^+ cooling. Moreover, HD^+ ions which decay by spontaneous emission are likely to decay stepwise into states with $v = 5, 6, 7$, rather than relaxing directly to $v = 0$. The inset of Fig. 2(a) shows that of these states, the $v = 5, 6$ states have a large PD cross-section at 313 nm. As a consequence, HD^+ ions which spontaneously decay from $v = 8$ before PD occurs may still be dissociated while transiting through the $v = 5, 6$ states. The 313 nm laser system detailed in Sect. 3.1.2 can provide enough power for efficient PD, and to simplify the detection scheme we choose to use the 313 nm cooling laser for PD rather than sending an additional 532 nm laser through the ion trap apparatus.

3.1.2 UV laser system for Be^+ cooling and PD

A schematic layout of the 313 nm laser for Be^+ cooling is depicted in Fig. 3. A commercial CW ring dye (Sulforhodamine B) laser oscillates at a single mode at 626 nm. About 0.6 W of output power is coupled into a single-mode optical fiber. After transmission by the fiber, the output laser beam is coupled into a bow-tie-shaped optical enhancement cavity housing a Brewster-cut beta barium borate (BBO) crystal. The enhancement cavity is kept resonant with the 626 nm laser frequency using the Hänsch–Couillaud scheme [24] in combination with negative feedback onto a piezo-mounted cavity mirror. In the BBO crystal, second-harmonic generation of 313 nm occurs, and the 313 nm radiation is coupled out of the enhancement cavity by the first cavity mirror it encounters, which is antireflection coated for 313 nm. In this way, up to 20 mW of 313 nm radiation is produced.

For laser cooling and detection of Be^+ the absolute wavelength of the 313 nm laser has to be tunable within a ∼1 GHz range with respect to the Be^+ $^2P_{3/2}(F = 3) \leftarrow {}^2S_{1/2}(F = 2)$ transition. To achieve absolute frequency stability, we pick off a small part of the dye laser output, and send it to a Fabry–Pérot cavity (FP1) having a free spectral range (δ_{FSR1}) of 149 MHz. The length of FP1 is controlled by a piezo-mounted mirror and stabilized to the wavelength of a helium–neon (HeNe) laser, which has a long-term absolute frequency stability of 1 MHz. An error signal for the servo loop (servo 1) is produced by modulating the length of FP1 in combination with synchronous demodulation of the output signal of a photodiode which measures the HeNe laser power transmitted by FP1. In the same way, the dye laser wavelength is stabilized to the length of FP1 through a servo loop (servo 2) with ∼0.1 s time constant. Orthogonal polarizations and polarizing beam splitter cubes are used to combine and separate the HeNe and dye laser beams running through FP1. In this configuration, FP1 acts as a transfer cavity to transfer the long-term frequency stability of the HeNe laser to the dye laser. To achieve tunability of the dye laser also in between the modes of FP1, we use a double-pass acousto-optic modulator (AOM) setup [25] in between the dye laser output and FP1 (Fig. 3). Thus, the frequency of the doubly-diffracted beam can be shifted continuously within the range $\Delta_{AOM} = \pm 100$ MHz, which exceeds δ_{FSR1}. Figure 3 explicitly shows the relationships between the various laser frequencies. A commercial wavelength meter is used to measure the dye-laser wavelength in order to lock the dye-laser frequency to the FP1 mode closest to the first subharmonic of the Be^+ $^2P_{3/2}(F = 3) \leftarrow {}^2S_{1/2}(F = 2)$ transition at 313 nm. It should be noted that the 200 MHz tuning range of the AOM translates to 400 MHz tuning range at 313 nm. Quasi-continuous tuning of the 313 nm frequency beyond the AOM tuning range is accomplished by relocking the double-passed output of the AOM to adjacent cavity modes of FP1.

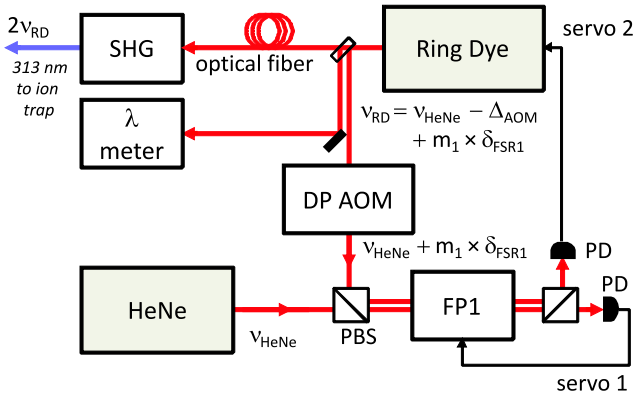

Fig. 3 Simplified schematic of the 313 nm laser setup used for Be^+ cooling and PD of HD^+. The setup involves a ring dye laser and a wavelength-stabilized helium–neon (HeNe) laser. The various acronyms denote the following components: DP AOM, double-pass acousto-optic modulator; PBS, polarizing beam splitter; FP1, Fabry–Pérot cavity; PD, photodiode; λ meter, wavelength meter; SHG, enhancement cavity for second-harmonic generation. The label m_1 attains integer values only. The HeNe and ring dye laser beams are overlapped before being coupled into FP1, but are drawn separately here for clarity. See Sect. 3.1.2 for details

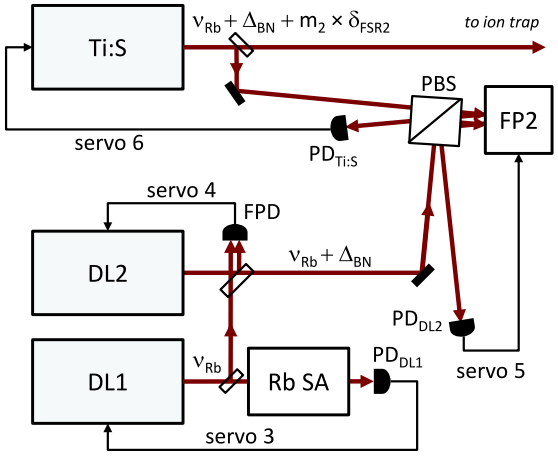

Fig. 4 Simplified schematic of the 782 nm laser setup used for excitation of the $(v' = 8, J' = 3) \leftarrow (v = 0, J = 2)$ vibrational overtone in HD^+. The setup involves one titanium:sapphire (Ti:S) laser and two diode lasers (DL1 and DL2). The various acronyms denote the following components: PBS, polarizing beam splitter; Rb SA, rubidium-vapor saturated absorption spectroscopy setup; FP2, Fabry–Pérot cavity; PD (PD_j), photodiode (for laser j); FPD, fast photodiode; BN, beat note between DL1 and DL2 recorded by FPD. The label m_2 attains integer values only. The beams of DL2 and the Ti:S laser are overlapped before being coupled into FP2, but are drawn separately here for clarity. See Sect. 3.1.3 for details

3.1.3 Near-infrared laser system for HD^+ spectroscopy

In Sect. 3.1, it was argued that a Ti:S laser is ideally suited for excitation of $v' = 8 \leftarrow v = 0$ vibrational overtones in HD^+ as it offers high output power and a wide tuning range. Similar to the spectral line recorded by Koelemeij et al., we expect each overtone to consist of many hyperfine components covering ∼150 MHz, with each hyperfine component being Doppler broadened to 10–20 MHz [3]. Therefore, with its sub-100 kHz linewidth, the Ti:S laser is sufficiently narrow to probe overtones without introducing additional broadening. Furthermore, a femtosecond frequency comb laser referenced to an accurate atomic clock can be used to control the absolute frequency of the Ti:S laser through an offset lock, and simultaneously measure the Ti:S frequency as done in [3]. However, a large part of the experimental work will not require the absolute frequency accuracy of the frequency comb; in such cases, it is sufficient if the Ti:S laser frequency is stable and tunable in a reproducible manner, without precise knowledge of its absolute frequency. To operate the setup independent of the frequency comb we have set up the system depicted in Fig. 4. A first diode laser (DL1) is locked to a hyperfine component of the Rb D1 line at 795 nm using saturated absorption spectroscopy (servo 3 in Fig. 4). Part of the output beam of DL1 is overlapped with part of the output beam of a second diode laser (DL2) at 795 nm, after which both are focused onto a fast photodiode to obtain the RF beatnote between DL1 and DL2. The beatnote signal is mixed with the RF output of a voltage-controlled oscillator (VCO, not shown in Fig. 4) using a double-balanced mixer. The difference frequency is subsequently converted to a voltage using a coax cable based Mach–Zehnder interferometer with a differential propagation delay time between the two arms of $\tau \approx 4$ ns [26]. The output voltage is subsequently amplified and integrated, and used to provide negative feedback to DL2. The effect of this arrangement (summarized as 'servo loop 4' in Fig. 4) is to stabilize the difference between the beatnote frequency, Δ_{BN}, and the frequency of the VCO, Δ_{VCO}, according to the relation [26]

$$(2\pi\,\Delta_{\mathrm{BN}})\tau = (2\pi\,\Delta_{\mathrm{VCO}})\tau + \frac{\pi}{2} \bmod 2\pi. \tag{9}$$

Thus, by adjusting Δ_{VCO} the frequency of DL2 is adjusted relative to DL1 and, therefore, relative to the Rb D1 line. The VCO used here has a tuning range of 400–1300 MHz. Figure 4 explicitly shows the relationships between the various laser frequencies.

The remaining part of the output of DL2 is sent to an FP cavity (FP2) built inside the Ti:S laser enclosure, which has a free spectral range $\delta_{\mathrm{FSR2}} = 0.75$ GHz. The length of FP2 can be varied using a piezo-mounted cavity mirror. Although the primary purpose of FP2 is to reduce the frequency drift and the linewidth of the free-running Ti:S laser by locking to the side of a fringe of FP2, we use FP2 also as a transfer cavity as follows. Employing orthogonal polarizations, we combine (using a polarizing beam splitter cube) the laser beam from DL2 with a beam picked off the main Ti:S output by a beamsplitter, and subsequently couple both into FP2 while separating the two reflected polarizations for individual analysis. Both reflections are used for side-of-the-fringe

locks: the reflection of the Ti:S beam is used to stabilize the Ti:S wavelength to the length of FP2 (servo 6), whereas the reflection of DL2 is used to lock the length of FP2 to the wavelength of DL2 via the piezo-mounted mirror (servo 5). Servo 5 is relatively slow (∼0.1 s time constant) to prevent any fast frequency fluctuations of DL1, DL2, or the VCO of being transferred to the Ti:S frequency. We use a wavelength meter to find the mode of FP2 closest to the $v' = 8 \leftarrow v = 0$ line of interest before locking the Ti:S to it. Then, with all servo loops closed, we can adjust the Ti:S frequency continuously and reproducibly (with respect to the frequency of DL1) over several hundreds of MHz simply by varying Δ_{VCO}. About 400 mW of Ti:S output power is focused to a 150 μm spot size, and overlapped with the 313 nm laser beam inside the ion trap (Sect. 3.2).

3.2 Ion trap apparatus and ion detection

We have set up an ion trap apparatus for confinement and laser cooling of several thousands of Be^+ ions. An ultra-high vacuum chamber (background vapor pressure 1×10^{-8} Pa) houses a linear radiofrequency (RF) trap consisting of four parallel molybdenum cylindrical rods of 4 mm radius and 60 mm length. Two diagonally opposing rods are segmented into 12 mm long parts, and capacitively coupled to RF ground. The other two rods are connected to the same phase of a high (∼250 V amplitude) voltage source at 13.3 MHz. The resulting RF field leads to ponderomotive confinement of ions in the radial direction. In the axial direction, confinement is achieved by a static positive voltage of 2–4 V applied to two pairs of diagonally opposing segmented electrodes (the endcap electrodes). In between each pair of endcap electrodes one segment (the center electrode) is kept at ≈0 V with respect to ground. The electrode circuitry is arranged such that the DC potentials of all electrodes can be individually adjusted. DC potentials are derived from an analog output board in the computer used to control the experiment. Home-built computer control software allows switching between individual adjustments of electrode voltages and adjustments of the various multipole terms of the trap's DC potential, which facilitates the compensation of electric fields due to charging of parts nearby the ions (see below). For the above trap parameters, a single-ion radial secular frequency of about 290 kHz is achieved for Be^+.

Be^+ ions are loaded into the trap by in situ electron impact ionization of neutral Be atoms, produced by an effusive atom source. Laser cooling of trapped Be^+ on the $^2P_{3/2}(F = 3) \leftarrow {}^2S_{1/2}(F = 2)$ transition (natural linewidth $2\pi \times 19.6$ MHz) is accomplished using the 313 nm laser system described in Sect. 3.1.2. The 313 nm laser beam is directed along the trap's symmetry axis, parallel to the quantization axis defined by a 0.3 mT static magnetic field. As a consequence, the circularly polarized laser induces primarily σ^+ transitions so that unwanted optical pumping and spontaneous emission into $^2S_{1/2}(F = 1)$ are minimized. The 313 nm beam waist is located at the position of the ions and amounts to 0.15 mm. Fluorescence photons emitted by Be^+ during laser cooling are collected by two independent sets of imaging optics with optical axes perpendicular to the trap axis. One optical system focuses the fluorescence onto a photomultiplier tube (PMT), whereas the second optical system images the laser-cooled ions onto an electron-multiplying charge-coupled device (EMCCD) camera. Images by the EMCCD camera reveal the presence and formation of Coulomb crystals. The resolution of the images is high enough to determine the spread of the individual ion images, which is directly related to the temperature of the secular motion. Comparing EMCCD images with the spread seen in artificial ion images at known temperature, produced by home-written molecular dynamics (MD) simulations, allows to determine the temperature of the Be^+ ions [27]. By comparing EMCCD images with MD images, also the ion number can be determined.

Stray electric fields are present in the trap, and the required DC compensation voltages range between 0 V and ±0.25 V, strongly depending on the fraction of the 20 μA filament emission current (used for loading of ions) that is collected by the electrode in question. Apparently, not all electrons are dissipated to ground through the DC voltage sources, and some electrons remain trapped on dielectric (oxide) layers on the electrode surfaces. Proper compensation voltages are found as follows. The ponderomotive confinement is modulated through the trap RF voltage, which leads to a synchronous modulation of the radial displacement of the Be^+ ions with respect to the 313 nm cooling laser beam if radially directed stray electric fields are present. By adjustment of electrode compensation voltages the displacement can be minimized. On time scales varying from one hour (during an experiment) to days (from experiment to experiment), the required compensation voltages typically fluctuate by 5%.

In our trap apparatus, we routinely produce Coulomb crystals containing over 3×10^3 Be^+ ions at temperatures (of secular motion) down to 5 mK. HD^+ molecular ions are loaded by in situ electron-impact ionization of neutral HD molecules in a background vapor (5×10^{-9} Pa partial pressure), created by introducing a small amount of HD gas to the vacuum chamber through a precision leak valve. The leak valve is motorized and computer controlled to improve the reproducibility of the loaded number of HD^+ ions. Electron impact ionization renders HD^+ ions in excited vibrational and rotational states. However, the molecule's permanent dipole moment facilitates spontaneous relaxation to $v = 0$, after which interaction with the ambient room-temperature blackbody radiation (BBR) field leads to a thermal distribution of population in the $J = 0$–5 rotational

states [28]. Using (7), we obtain vibrationally excited state lifetimes of 12–55 ms, and therefore vibrational relaxation should take place within less than one second.

The secular motion of the HD^+ ions is sympathetically cooled to a temperature similar to that of the Be^+ ions [29]. Because of their larger charge-to-mass ratio, HD^+ ions accumulate near the trap axis, which manifests itself as a dark core appearing inside the Be^+ Coulomb crystal [29]. A measure of the number of HD^+ ions can be obtained by excitation of the HD^+ secular motion using an external RF electric field, resonant with the radial center-of-mass (COM) motion of the HD^+ ions. In our setup, we apply this field by adding a suited RF voltage to one of the center electrode potentials. For red detunings much larger than the natural linewidth of the 313 nm cooling transition, the motionally driven HD^+ ions heat the surrounding Be^+ ions, leading to increased interaction with the 313 nm cooling laser and therefore to increased fluorescence levels [29]. Sweeping the frequency of the RF driving field across the secular COM-mode frequency results into a resonance visible in the 313 nm fluorescence, with a peak height proportional to the number of trapped ions (see Fig. 5). Furthermore, with this method of detection by secular excitation, COM mode frequencies of unknown trapped species can be determined which allows to identify trapped molecular ions by their charge-to-mass ratio [29]. Besides Be^+ (mass 9 amu) and HD^+ (mass 3 amu) we have observed trapped and sympathetically cooled species with mass 2 amu (H_2^+ and D^+), mass 3 amu (H_3^+), mass 4 amu (H_2D^+), and mass 10 amu (BeH^+).

3.3 Laser excitation of the $(v' = 8, J' = 3) \leftarrow (v = 0, J = 2)$ overtone and detection by secular excitation

We employ the following procedure to observe the $(v' = 8, J' = 3) \leftarrow (v = 0, J = 2)$ overtone in HD^+. First, we load 2×10^3 Be^+ ions into the trap while laser cooling with 10 mW of 313 nm power in a 0.15 mm spot size and ∼250 MHz red detuning. This relatively large irradiance is chosen to ensure efficient PD of HD^+ in $v = 8$. Note that at this stage the 782 nm laser had already been tuned close to the transition wavelength predicted by Moss [23], and that the 782 nm beam is still blocked by a mechanical shutter. Next, 2×10^2 HD^+ ions are added to the Be^+ sample. During loading of HD^+, some of the neutral HD molecules react with Be^+ ions in the $^2P_{3/2}$ state to produce BeH^+ or BeD^+. These ions are expelled from the trap by temporarily applying a DC quadrupole deformation of the trap potential [30].

During the next 4 s, we sweep the frequency of the RF field used for secular excitation across the HD^+ COM motional resonance near 830 kHz while recording the PMT fluorescence signal. During this period the HD^+ internal degrees of freedom are supposed to thermalize with the ambient 300 K BBR field. Next, we set the VCO of the 782 nm laser system to the desired frequency and open the 782 nm shutter for 10 s. To increase the total number of photodissociated HD^+ ions (and thus the signal-to-noise ratio) we Doppler-broaden the line by tuning the 313 nm laser closer to resonance (∼−50 MHz) just before opening the shutter, thereby heating both the Be^+ and HD^+ to 0.1 K (as judged from the comparison of EMCCD images with MD simulations). At this temperature, the hyperfine structure is no longer well resolved, and the 782 nm laser will therefore address most HD^+ ions in the $(v = 0, J = 2)$ state, irrespective of their hyperfine state. The resulting enhancement of the signal-to-noise ratio was useful during the initial search for

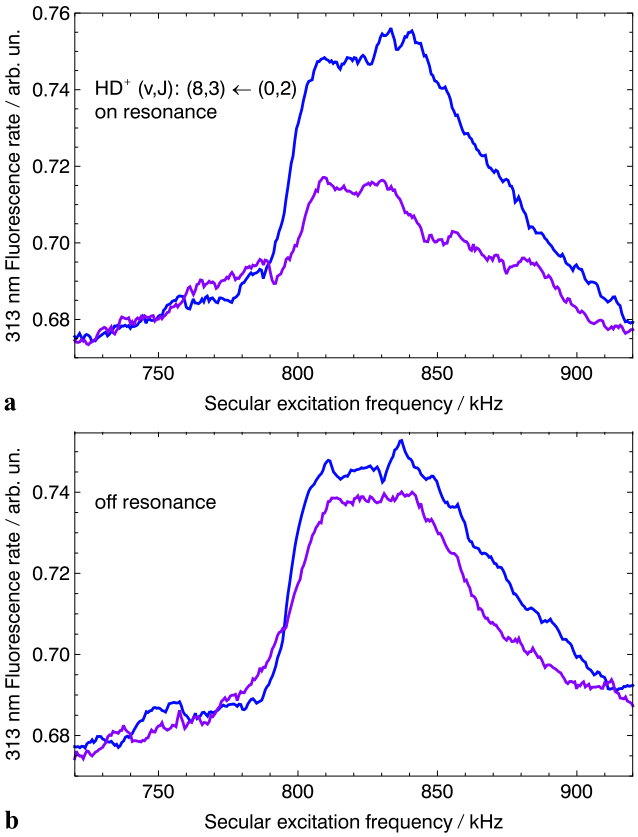

Fig. 5 (**a**) 313 nm fluorescence traces recorded using the PMT while sweeping the frequency of an RF electric field used for exciting the secular motion of the HD^+ ions. Sweep direction is towards higher frequencies. The raw signal data were smoothed using an exponential moving average to remove high-frequency electronic noise. The peak height of the resonance in the PMT signal roughly corresponds to the number of trapped HD^+ ions. The *upper curve* was taken in the course of 4 s before probing the ions with both the 782 nm and 313 nm lasers for 10 s; the *lower curve* was taken in 4 s immediately afterwards. The 782 nm was tuned to resonance with the $(v' = 8, J' = 3) \leftarrow (v = 0, J = 2)$ overtone transition, and the loss of ∼50% of the initial number of HD^+ ions is almost entirely due to REMPD. (**b**) Same as in (**a**), but now with the 782 nm tuned away from resonance by 100 MHz. The loss of ∼10% of the initial number of HD^+ ions is consistent with the expected losses due to chemical reactions of HD^+ with background-vapor constituents [18]. See Sect. 4 for details

the $(v' = 8, J' = 3) \leftarrow (v = 0, J = 2)$ transition. After the 10 s period of REMPD we close the 782 nm shutter, tune the 313 nm laser back to 250 MHz red detuning, and consecutively record the 313 nm fluorescence level while applying a second 4 s secular excitation sweep.

4 Results and discussion

Figure 5 shows traces of the 313 nm fluorescence signal versus HD^+ secular excitation frequency. In Fig. 5(a), the Ti:S laser frequency was tuned to the center of the $(v' = 8, J' = 3) \leftarrow (v = 0, J = 2)$ line. The transition frequency as deduced from the wavelength meter agrees with that calculated by Moss within the 0.2 ppm accuracy achievable at this preliminary stage of the experiment. From the height difference between the two resonances we estimate that about 50% of the HD^+ were lost during the 10 s period of REMPD. Part of this loss may be induced by collisions of HD^+ with neutral HD and H_2 molecules in the background vapor, which lead to the formation of trihydrogen molecular ions. To distinguish this effect from the losses due to REMPD, we detuned the Ti:S by 100 MHz and repeated the measurement (Fig. 5(b)). In this case, a smaller HD^+ loss of about 10% was observed, which is consistent with the background losses seen under similar conditions in other experiments [18]. The same loss was also observed with the 782 nm tuned away from resonance by much more than 100 MHz, on either side of the resonance. The results shown in Fig. 5 are reproducible and evidence excitation of the $(v' = 8, J' = 3) \leftarrow (v = 0, J = 2)$ resonance and subsequent PD by 313 nm. Reducing the 313 nm power to 70 μW greatly reduced the temperature achieved by laser cooling, but in this case the power was too low to induce observable REMPD losses. Therefore, in the next phase of the experiment we plan on inducing PD by a third laser beam at 532 nm, so that spectra can be taken at low temperatures and, consequently, with minimum Doppler broadening.

The question arises whether the large irradiance required for excitation of the $v' = 8 \leftarrow v = 0$ overtone could possibly induce appreciable PD or dynamic Stark shifts. We found no evidence for PD by 782 nm, which was tested by reducing the 313 nm power to 70 μW as described above. With the aid of (8) we find that the $v = 8$ cross-section for PD by 782 nm is about 6×10^{-21} cm^2. For the 782 nm irradiance levels used in our experiment, the PD-limited lifetime of $v = 8$ molecules is 35 ms, which is considerably longer than the 12 ms spontaneous lifetime. This explains why no $(1 + 1)$ REMPD by 782 nm alone is observed.

The 782 nm laser beam will nevertheless induce a dynamic Stark shift of $v = 8$ due to off-resonant coupling to the $2p\sigma_u$ dissociation continuum. To estimate the size of this effect, we use the following expression to obtain the shift (in Hz) [31]:

$$\Delta_{vJ}(E) = \frac{1}{2\pi E} PV \int_0^\infty \frac{\sigma_{vJ}(E')}{E - E'} \, \mathrm{d}E'. \tag{10}$$

Here, PV denotes the Cauchy principal value, and $\sigma_{vJ}(E)$ is defined by (8). We emphasize that this expression can only provide an order-of-magnitude estimate of the dynamic Stark shift since the cross-sections $\sigma_{vJ}(E)$ are averages over magnetic substates M [19], whereas dynamic Stark shifts should be evaluated for individual (v, J, M) states. Using (10), we obtain a negative shift to the $v = 8$ energy level of order -10 kHz. Relative to the transition frequency, this shift contributes at the level of 3×10^{-11}, i.e., far below the target accuracy of the present experiment.

5 Outlook

In the experiment described in [3], the center frequency of the $(v' = 4, J' = 3) \leftarrow (v = 0, J = 0)$ spectrum, which was Doppler-broadened to a linewidth ∼50 MHz, was determined with an instrument resolution of 0.45 MHz. The observed Doppler broadening was attributed to the relatively high (50 mK) temperature of the HD^+ ions as well as to excess micromotion at the trap RF frequency. The present experiment is designed for lower temperature and reduced micromotion amplitudes, and we expect that spectroscopy of $v' = 8 \leftarrow v = 0$ overtones at 782 nm may be done with 0.2 MHz resolution, or 0.5 ppb. The analysis of systematic shifts to the $(v' = 4, J' = 3) \leftarrow (v = 0, J = 2)$ transition in [3], as well as recent studies of the Zeeman effect of HD^+ [9, 16] and the blackbody radiation induced ac-Stark effect [15], furthermore point out that uncertainties associated with these systematic effects are smaller than 10 kHz. We believe that this also holds true for the $v' = 8 \leftarrow v = 0$ overtones, with the largest contribution stemming from the dynamic Stark shift due to the 782 nm laser.

Hyperfine substructure in the rovibrational lineshape is another possible source of inaccuracy. Hyperfine level splittings may be calculated with less than 50 kHz accuracy [10, 11], and the theoretical hyperfine structure may be included in the lineshape fit function [3]. From the fit, the center of gravity of the spectrum can be determined, which corresponds to the deperturbed rovibrational transition frequency. The uncertainty of such a theoretical lineshape function is expected to affect the determination of the deperturbed rovibrational frequency far below the 50 kHz level, as the differential nature of measurement of transition frequencies leads to partial cancelation of systematic errors in the hyperfine level energies. Furthermore, errors in the position of hyperfine subcomponents in the spectrum will affect the accuracy only at a fraction of their value, as the sum of errors of all

hyperfine subcomponents does not shift the center of gravity of the spectrum.

Assuming that the frequency of a single line $v' = 8 \leftarrow v = 0$ can be measured with 0.5 ppb accuracy, and that a comparison can be made with accurate theoretical results to extract m_p/m_e, we can find the resulting uncertainty in m_p/m_e as follows. We use (1) with a slightly different reduced mass μ due to a hypothetical change of the proton mass to find the corresponding energy level shift (note that within the Born–Oppenheimer approximation this mass variation is assumed to have no effect on the $1s\sigma_g$ potential $V_1(R)$). Expressing energy shifts in terms of frequency shifts, $\delta\nu$, we thus find dimensionless sensitivity coefficients for the transition frequencies, $\eta^{pe}_{vv'JJ'}$, defined as

$$\frac{\delta(m_p/m_e)}{m_p/m_e} = \eta^{pe}_{vv'JJ'} \frac{\delta\nu_{vv'JJ'}}{\nu_{vv'JJ'}}. \tag{11}$$

We obtain $\eta^{pe}_{0823} = 2.665$ and $\eta^{pe}_{0423} = 2.282$. The latter value may be compared with the more accurate sensitivity coefficients available from [32], and agreement to within 10^{-3} is found. We can now plot the obtainable relative uncertainty in m_p/m_e versus the theoretical and experimental fractional uncertainties ($\delta\nu_{\rm theo}/\nu_{vv'JJ'}$ and $\delta\nu_{\rm exp}/\nu_{vv'JJ'}$, respectively) by use of the equation

$$\frac{\delta(m_p/m_e)}{m_p/m_e} = \eta^{pe}_{vv'JJ'} \frac{\sqrt{(\delta\nu_{\rm theo})^2 + (\delta\nu_{\rm exp})^2}}{\nu_{vv'JJ'}}. \tag{12}$$

Such a contour plot for $v' = 8 \leftarrow v = 0$ is shown in Fig. 6.

In a similar manner, we establish that the deuteron–proton mass ratio m_d/m_p does not play an important role. To see this, we again modify (1), this time to find the sensitivity coefficient $\eta^{dp}_{vv'JJ'}$. Combining the result $\eta^{dp}_{0823} = 7.99$ with the 0.1 ppb uncertainty of the 2010 CODATA recommended value of m_d/m_p, we find that this translates to an effect at the level of 5 kHz. The relative insensitivity to m_d/m_p is not surprising as it has been shown that in the Born–Oppenheimer approximation $\eta^{dp}_{vv'JJ'}/\eta^{pe}_{vv'JJ'} \approx 3$, independent of the transition that is being considered [32].

With theoretical calculations approaching 0.3 ppb [1], and assuming 0.5 ppb accuracy for the measurement of a single overtone, we may determine m_p/m_e with an accuracy of 1.6 ppb (Fig. 6). The measurement accuracy is expected to be limited predominantly by random measurement noise. However, in Sect. 3.1.1 it was pointed out that eleven $(v' = 8, J') \leftarrow (v = 0, J)$ overtones are accessible at different wavelengths, which would improve statistics and enable the determination of m_p/m_e at the level of 0.9 ppb. This value would then be largely limited by the theoretical uncertainty. Moreover, also overtones involving $v = 7$ and $v = 9$ are within the range of the Ti:S laser system, and together with an improvement of the theoretical accuracy by a factor of three, a new value m_p/m_e with accuracy

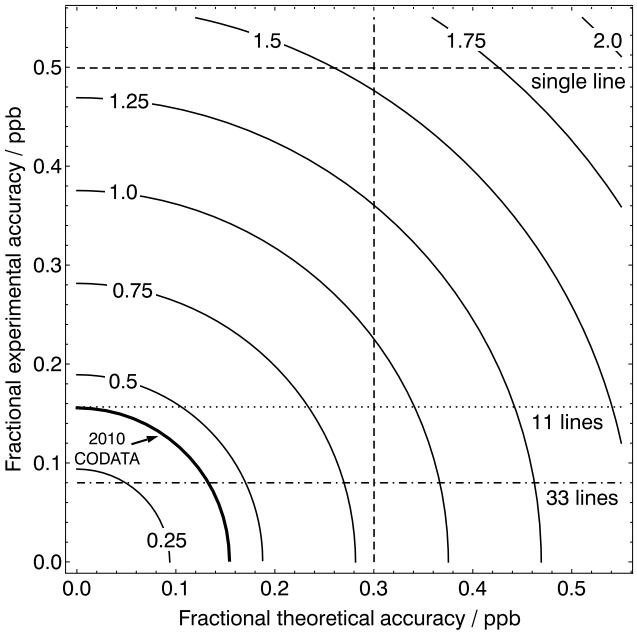

Fig. 6 Contour plot of the accuracy (in ppb) of the value of m_p/m_e versus the accuracy of the input used for its determination, which in this case will consist of theoretically and experimentally determined $v' = 8 \leftarrow v = 0$ transition frequencies. The *bold contour* indicates the accuracy of the 2010 CODATA recommended value. The *vertical dashed line* indicates the current state of the art in theoretical calculations [1], and *horizontal lines* show the projected accuracy achievable with the present experimental setup after measurement of a single rovibrational line $v' = 8 \leftarrow v = 0$, 11 different rovibrational lines within the $v' = 8 \leftarrow v = 0$ manifold, and 33 different rovibrational lines within the $v' = 9, 8, 7 \leftarrow v = 0$ manifolds, respectively (see Sect. 5 for details)

0.36 ppb would be possible, thereby significantly improving on the 2010 CODATA recommended value. Finally, we emphasize that the determination of m_p/m_e through theoretical calculations and spectroscopy of HD^+ represents a direct method to retrieve m_p/m_e, in contrast to the 2010 CODATA value of m_p/m_e which is determined largely by individual mass measurements. Furthermore, both methods involve high-accuracy QED calculations, but appertain to vastly different systems (QED of a molecule versus QED of bound-electron g-factors). Comparison of the value of m_p/m_e obtained from HD^+ with the CODATA value therefore constitutes a consistency check of QED in general.

Acknowledgements J.C.J.K. acknowledges support from the Netherlands Organisation for Scientific Research (NWO). M.A.H acknowledges support from the Ministry of Science and Technology of Iran.

References

1. V.I. Korobov, Phys. Rev. A **77**, 022509 (2008)
2. W.H. Wing, G.A. Ruff, W.E. Lamb Jr., J.J. Spezeski, Phys. Rev. Lett. **36**, 1488 (1976)
3. J.C.J. Koelemeij, B. Roth, A. Wicht, I. Ernsting, S. Schiller, Phys. Rev. Lett. **98**, 173002 (2007)
4. J.-Ph. Karr, L. Hilico, V.I. Korobov, Can. J. Phys. **89**, 103 (2011)
5. C.W. Chou, D.B. Hume, J.C.J. Koelemeij, D.J. Wineland, T. Rosenband, Phys. Rev. Lett. **104**, 070802 (2010)
6. R.S. Van Dyck Jr., D.L. Farnham, S.L. Zafonte, P.B. Schwinberg, in *Trapped Charged Particles and Fundamental Physics*, ed. by D.E. Dubin, D. Schneider. AIP Conf. Proc., vol. 457 (AIP, Woodbury, 1999), p. 101
7. A. Solders, I. Bergström, Sz. Nagy, M. Suhonen, R. Schuch, Phys. Rev. A **78**, 012514 (2008)
8. J. Verdú, S. Djekić, S. Stahl, T. Valenzuela, M. Vogel, G. Werth, T. Beier, H.-J. Kluge, W. Quint, Phys. Rev. Lett. **92**, 093002 (2004)
9. D. Bakalov, V.I. Korobov, S. Schiller, Phys. Rev. A **82**, 055401 (2010)
10. D. Bakalov, V.I. Korobov, S. Schiller, Phys. Rev. Lett. **97**, 243001 (2006)
11. V.I. Korobov, L. Hilico, J.-Ph. Karr, Phys. Rev. A **79**, 012501 (2009)
12. B.D. Esry, H.R. Sadeghpour, Phys. Rev. A **60**, 3604 (1999)
13. J. Brown, A. Carrington, *Rotational Spectroscopy of Diatomic Molecules*, 1st edn. (Cambridge University Press, Cambridge, 2003)
14. R.C. Hilborn, Am. J. Phys. **50**, 982 (1982)
15. J.C.J. Koelemeij, Phys. Chem. Chem. Phys. (2011). doi:10.1039/C1CP21204D
16. D. Bakalov, V.I. Korobov, S. Schiller, J. Phys. B, At. Mol. Opt. Phys. **44**, 025003 (2011)
17. E.A. Colbourn, P.R. Bunker, J. Mol. Spectrosc. **63**, 155 (1976)
18. B. Roth, J.C.J. Koelemeij, H. Daerr, S. Schiller, Phys. Rev. A **74**, 040501 (2006)
19. G.H. Dunn, Phys. Rev. **172**, 1 (1968)
20. M. Tadjeddine, G. Parlant, Mol. Phys. **33**, 1797 (1977)
21. N.P.F.B. van Asselt, J.G. Maas, J. Los, Chem. Phys. **11**, 253 (1975)
22. S. Kilic, Ph.D. thesis, Université Paris VI (2005)
23. R.E. Moss, Mol. Phys. **78**, 371 (1993)
24. T.W. Hänsch, B. Couillaud, Opt. Commun. **35**, 441 (1980)
25. E. Donley, T. Heavner, S.R. Jefferts, Rev. Sci. Instrum. **60**, 3604 (2005)
26. U. Schünemann, H. Engler, R. Grimm, M. Weidemüller, M. Zielonkowski, Rev. Sci. Instrum. **70**, 242 (1999)
27. C.B. Zhang, D. Offenberg, B. Roth, M.A. Wilson, S. Schiller, Phys. Rev. A **76**, 012719 (2007)
28. J.C.J. Koelemeij, B. Roth, S. Schiller, Phys. Rev. A **76**, 023413 (2007)
29. P. Blythe, B. Roth, U. Fröhlich, H. Wenz, S. Schiller, Phys. Rev. Lett. **95**, 183002 (2005)
30. B. Roth, P. Blythe, S. Schiller, Phys. Rev. A **75**, 023402 (2007)
31. C. Cohen-Tannoudji, J. Dupont-Roc, G. Grynberg, *Atom–Photon Interactions*, 1st edn. (Wiley, New York, 1992)
32. S. Schiller, V. Korobov, Phys. Rev. A **71**, 032505 (2005)